

This is the final peer-reviewed accepted manuscript of:

**Debbie J. Dupuis, Luca Trapin. (2023). "Mixed-frequency extreme value regression: Estimating the effect of mesoscale convective systems on extreme rainfall intensity". *Annals of Applied Statistics*, Vol. 17, Issue 2, June 2023, Pages 1398-1418.**

The final published version is available online at:

<https://doi.org/10.1214/22-AOAS1675>

#### Terms of use:

Some rights reserved. The terms and conditions for the reuse of this version of the manuscript are specified in the publishing policy. For all terms of use and more information see the publisher's website.

*This item was downloaded from IRIS Università di Bologna (<https://cris.unibo.it/>)*

***When citing, please refer to the published version.***

# MIXED-FREQUENCY EXTREME VALUE REGRESSION: ESTIMATING THE EFFECT OF MESOSCALE CONVECTIVE SYSTEMS ON EXTREME RAINFALL INTENSITY

BY DEBBIE J. DUPUIS<sup>1,a</sup> AND LUCA TRAPIN<sup>2,b</sup>

<sup>1</sup>*Department of Decision Sciences, HEC Montréal, 3000, chemin de la Côte-Sainte-Catherine, Montréal (Québec) H3T 2A7, Canada <sup>a</sup>[debbie.dupuis@hec.ca](mailto:debbie.dupuis@hec.ca)*

<sup>2</sup>*Department of Statistics, University of Bologna, Via delle Belle Arti 41, 40126 Bologna, Italy <sup>b</sup>[luca.trapin@unibo.it](mailto:luca.trapin@unibo.it)*

Understanding and modeling the determinants of extreme hourly rainfall intensity is of utmost importance for the management of flash flood risk. Increasing evidence shows that mesoscale convective systems (MCS) are the principal driver of extreme rainfall intensity in the United States. We use extreme value statistics to investigate the relationship between MCS activity and extreme hourly rainfall intensity in Greater St. Louis, an area particularly vulnerable to flash floods. Using a block maxima approach with monthly blocks, we find that the impact of MCS activity on monthly maxima is not homogeneous within the month/block. To appropriately capture this relationship, we develop a mixed-frequency extreme value regression framework accommodating a covariate sampled at a frequency higher than that of the extreme observation.

**1. Introduction.** All regions of the contiguous<sup>1</sup> United States have experienced an increase in rainfall intensities since the 1950s, see [Kunkel et al. \(2013\)](#) for increases to 1-day and 2-day totals, and [Barbero et al. \(2017\)](#) for increases to 1-hour maxima. Increased precipitation, along with increased population and wealth, have lead to increases in flood damages ([Pielke Jr and Downton, 2000](#)). Compiling a data-base of fatalities associated with flooding events from 1959 to 2005, [Ashley and Ashley \(2008\)](#) find no significant decrease in flood risk despite technological advancements in watch-warning and detection systems. Atmospheric science suggests that climate change should further increase rainfall intensities much faster than the total precipitation amount ([Trenberth et al., 2003](#)) and recent global climate models and regional climate models point in this direction, see [Prein et al. \(2017\)](#) for the US and [Kendon, Blenkinsop and Fowler \(2018\)](#) for the UK.

Extreme short time-span rainfall intensity (e.g. very large mm/hour) is a main driver of flash floods and a major threat in the US. Flash floods are the “#1 weather-related killer in the United States!” ([Service, 2022](#)). More than 28,000 flash flood events were reported across the US over 2007–2015 ([Gourley et al., 2017](#)) and the problem is likely to worsen in a changing climate with heavier precipitation ([MassonDelmotte et al., 2021](#)). Proper design of hydraulic structures and flood-protection infrastructure critically depends on the successful modeling of extreme hourly rainfall intensity dynamics ([Callau Poduje and Haberlandt, 2017](#)).

Several geographic and atmospheric factors contribute to the non-stationary behavior of extreme hourly rainfall. Across sites, differences in rainfall can be partially explained by longitude, latitude, and elevation, see e.g. [Tye and Cooley \(2015\)](#) and [Sebille, Fougères and Mercadier \(2017\)](#) where these covariates are included to explain annual maximum daily rainfall at locations in the US and France, respectively. In the US, rainfall (daily and hourly) is further partially explained by the Southern Oscillation Index (SOI) and the Pacific Decadal

---

*Keywords and phrases:* extreme value regression, mesoscale convective systems, mixed-frequency data, rainfall intensity.

<sup>1</sup>The lower 48 states in North America (including the District of Columbia).

Oscillation (PDO), see e.g. [Ouarda, Yousef and Charron \(2019\)](#). Temperature also partially explains precipitation, but the relationship is complex, and its effect on precipitation extremes is difficult to separate from the combined effects of multiple atmospheric variables, see e.g. [O’Gorman \(2012\)](#). Summer rainfall in the US has another important driver: Mesoscale Convective Systems (MCS). MCS are the largest convective clouds that can be identified by satellite infrared imagery of a large, contiguous precipitation area of 100 km in at least one direction. They are often found downwind of mountain ranges and are responsible for about 60 percent of summer rainfall in the Great Plains ([Nesbitt, Cifelli and Rutledge, 2006](#)) and a majority of extreme rainfall east of the Rocky Mountains ([Stevenson and Schumacher, 2014](#)). [Feng et al. \(2016\)](#) show that the increases in springtime extreme rainfall in the Central United States are dominated by MCS. The accurate simulation of MCS, and the ensuing extreme rainfall, is necessary to evaluate changes in response to climate change.

The scientific community uses global climate models (GCM) to project climate into the future. GCM are based on mathematical equations that characterize how energy and matter interact in different parts of the ocean, atmosphere, and land. They use a three-dimensional grid of cells to represent the Earth’s surface and they are solved at given time steps (minutes, hours, days, or years). GCM have to parametrize deep convection due to their coarse grid spacing. This leads to large uncertainties and model biases, and GCM are typically considered unreliable at sub-daily time scales ([Westra et al., 2014](#)). Regional climate models account for topography, land-cover distribution, etc, to provide information at finer, sub-GCM grid scales.

[Prein et al. \(2020\)](#) investigate the ability of a regional convection-permitting climate model (CPM) to reproduce the size, precipitation rate, propagation speed, and lifetime of the observed MCS. A CPM is a high-resolution ( $\leq 4$  km) model that allows an explicit simulation of deep convection, and an improved representation of fine-scale orography and variations of surface fields. [Prein et al. \(2020\)](#) show that the model has notably the poorest reproducibility in the US Midwest in July, where the number of MCS, mean precipitation, and percentage of precipitation from tracked MCS are particularly biased (see their Figures 8b, 8f, and 8j). [Feng et al. \(2021\)](#) also evaluate MCS in CPM simulations. Their simulations show the largest number of MCS, largest MCS precipitation, and largest % MCS precipitation in Missouri and neighboring western states (see Figure 5 of [Feng et al. \(2021\)](#)), but they are inadequate. Simulations most consistently and substantially underestimate all three quantities in Missouri (see Figures 6 and 7 of [Feng et al. \(2021\)](#)).

[Fowler, Wasko and Prein \(2021\)](#) state “... understanding the processes driving change in various climate zones and their variations on regional scales is vital in advancing the projection of rainfall extremes” and “There remains a need for continued investigations and improved understanding of mechanisms that cause changes in subdaily extreme rainfalls, which will only be possible by dedicated observational efforts merged with further development of CPMs.” This paper is a dedicated observational effort for greater St. Louis, an area at the heart of the US Midwest region poorly reproduced by existing CPMs. Our aim is to study the MCS impact on extreme hourly rainfall intensity within an extreme value regression model to uncover local relationships that can be used to improve CPMs.

In climate science, rainfall extremes are events greater than some extreme threshold (90th, 95th, or 99th percentile of the distribution) and it is natural to think in terms of threshold exceedances. Conversely, it is more natural to look at block maxima, e.g. annual maxima, when estimating the more infrequent events required for engineering design: Intensity-Duration-Frequency (IDF) curves are established based on identification of maximum yearly values for different durations, e.g. from 5 to 1440 minutes, see [Koutsoyiannis, Kozonis and Manetas \(1998\)](#). The Generalized Extreme Value (GEV) distribution is the workhorse of analyses of block maxima in hydrology and continues to serve as the building block for methodological innovations: see [Asadi, Engelke and Davison \(2018\)](#) on annual maxima of river

discharges, [Zhu, Liu and Lund \(2019\)](#) on annual minima of daily temperatures, [Carreau and Toulemonde \(2020\)](#) on annual maxima of daily precipitation data, amongst others. There is a very large and long-standing literature on examining annual maximum daily precipitation, however studies of sub-daily precipitation extremes are more recent, see [Barbero et al. \(2019\)](#) and references therein.

This paper considers monthly maximum hourly rainfall as a measure of extreme rainfall intensity in the greater St. Louis, Missouri area. We collect hourly MCS observations in the form of a binary variable indicating the presence/absence of an MCS at one location, and use this information to build the monthly MCS frequency. Exploratory data analysis in Section 2 suggests this variable is strongly related to the size of monthly maximum hourly rainfall, and one could thus build an extreme value regression model ([Beirlant et al., 2004](#)) tying monthly maxima to the monthly MCS frequencies. This does not however necessarily make the most efficient use of the available MCS information. MCS have known diurnal characteristics ([Carbone and Tuttle, 2008](#)) and these may hide more complex patterns in the MCS-rainfall relationship. Exploratory data analysis in Section 2 suggests that monthly MCS frequencies computed for each hour of the day contribute unevenly to the dynamics of monthly maxima. An appropriate extreme value regression model would then require tying the monthly maximum hourly rainfall to a covariate sampled 24 times within the block, i.e. monthly MCS frequencies per each hour of the day.

There are currently no extreme value regression models available to study how the extremes of  $y$  sampled at a certain frequency depend on a variable  $x$  sampled at a higher frequency. Common practice suggests aggregating  $x$  to the same frequency as the extreme of  $y$ , but this convention makes inefficient use of the available information, and in the case of our data, drowns important dynamics. We develop a class of regression models for extreme value analysis that accommodate observations sampled at different frequencies. We propose a flexible, data-driven aggregation scheme that is proper to the extreme value context, and captures the important dynamics in our monthly maximum hourly precipitation. Our new model is a good fit to the data and reveals important previously unidentified dynamics. Our model could easily check that observed relationships are borne out by CPM simulated data, helping to improve the representation of relationships in CPM, and providing an additional tool to assess hydrologic hazards within the non-stationary framework.

The remainder of the paper is organized as follows: Section 2 presents the dataset of hourly rainfall and MCS records; Section 3 outlines our novel mixed-frequency extreme value regression framework; Section 4 shows how our mixed-frequency GEV model is able to uncover the impact of MCS on extreme rainfall intensity; Section 5 concludes. Appendices provide data information, the general form of our mixed-frequency GEV model, as well as a simulation study.

**2. Dataset.** The city of St. Louis sits on the banks of the Mississippi and Missouri rivers. Excessive amounts of water from the many tributaries of these rivers leave the city particularly vulnerable to flooding. In 2019, heavy rains on frozen ground, followed by more heavy rain through the spring, left the city and a record number of counties in the U.S. Midwest under water for several months in the Great Flood of 2019 ([Almukhtar et al., 2019](#)). The region previously suffered the Great USA Flood of 1993 ([Larson, 1996](#)). The city’s troubles are however not limited to river floods. Pluvial flash floods caused by extreme short time-span rainfall intensity are more frequent ([News, 2018](#); [Davies, 2014a,b, 2017](#)). The Missouri River Valley is identified as one of the six “hot spots” for flash floods in the U.S. based on 1981-2010 data ([Saharia et al., 2017](#)) and the state of Missouri suffered approximately 3000 flash floods during 1996-2017 ([Ahmadalipour and Moradkhani, 2019](#)).

[Feng et al. \(2016\)](#) found that many states in the U.S. Midwest experienced 0.4-0.8 mm/day (roughly 20-40%) per decade increases in total MCS rainfall over the period of study, so the

area has already been flagged as interesting from an MCS perspective. We use the MCS database produced by the [Feng et al. \(2016\)](#) study and obtained from these authors. Data are available for the months of April to August from 1979-04-01 00:00:00 to 2014-08-31 23:00:00 UTC. Following [Prein et al. \(2017\)](#) and [Prein et al. \(2020\)](#), we focus on the warmest months, June, July and August (JJA). We show the data in local standard time to favor interpretability. For each pixel location<sup>2</sup> shown in Figure 1, we retrieve the hourly precipitation measured in millimeters and a binary variable recording whether or not the pixel location was part of an MCS at that hour. In these data, MCS are responsible for 43%, 38%, and 32% of the rainfall in June, July, and August, respectively. Moreover, these levels rise to 49%, 43%, and 46% (62%, 55%, and 48%), if one considers quantities exceeding the 95th (99th) quantile of total rainfall, in June, July, and August, respectively.

Fig 1: **Data.** Grid of filled circles show the 35 pixel locations included in our analysis.



As indicated in the introduction, we use monthly maximum hourly precipitation as a measure of extreme hourly rainfall intensity. Let  $\tilde{y}_{hd}^t$  be the rainfall in millimeters at the  $h$ th hour of the  $d$ th day in the  $t$ th month at any location, with  $h \in \{1, \dots, 24\}$ ,  $d \in \{1, \dots, D_t\}$ ,  $t \in \{1, \dots, 108\}$ , the monthly maxima are defined as

$$y_t = \max_{h,d} \left\{ \left\{ \tilde{y}_{hd}^t \right\}_{h=1}^{24} \right\}_{d=1}^{D_t}.$$

We explore the properties of this time series of maxima at each location and find that monthly maximum hourly precipitation has drastically increased over time, showing an average size across locations of 12.28 mm/hour (st.dev. 5.73) over the period 1997-2014 compared to an

<sup>2</sup>Table 2 in Appendix A gives the longitude and latitude coordinates of the pixels.

average size across locations of 9.13 mm/hour (st.dev. 4.45) during the years 1979-1996<sup>3</sup>. During the warm season, midlatitude regions like the Missouri River Valley often experience the highest rainfall intensity in the late afternoon when precipitation is related to small-scale thermodynamic processes affecting surface temperature and vertical static stability (Dai and Trenberth, 2004; Evans and Westra, 2012). Hourly rainfall intensity over land, in general, is often locked into a diurnal cycle and other factors such as weather types (Moron et al., 2019), topographical conditions (Li, 2017), or propagation of moist convection (Ploshay and Lau, 2010) can make the intensity peak at different times of the day. To investigate further, we henceforth examine data for June, July, and August, separately. Figure 2 shows the time of the day at which the monthly maximum hourly precipitation was observed, pooling observations across locations. We show the timing for the 1979-1996 and 1997-2014 periods to highlight the shift that has occurred. In all three months, maxima have moved away from the overnight period<sup>4</sup>. The timing distribution over the 1997-2014 period is actually quite similar for the three months, with the late afternoon and evening periods being more prosperous than the first half of the day.

To measure MCS activity we consider the MCS frequency. As MCS frequency has increased, and could more than triple in North America by the end of the 21st century (Prein et al., 2017), our interests lie in the role of the MCS frequency in explaining monthly maximum hourly precipitation. Let  $\tilde{x}_{hd}^t$  be the binary variable recording the presence/absence of an MCS at the  $h$ th hour of the  $d$ th day in the  $t$ th month at any location, we define the monthly MCS frequency as

$$x_t = \frac{1}{24D_t} \sum_{d=1}^{D_t} \sum_{h=1}^{24} \tilde{x}_{hd}^t.$$

Figure 3 indicates that monthly maximum hourly rainfall is strongly and positively related to the monthly MCS frequency for all three months. This was anticipated since high proportions of MCS favor more intense storms (Barbero et al., 2019) and cloud-cloud interactions. The convective field as a whole acquires a memory of past precipitation and inter-cloud dynamics, leading to more extreme precipitation (Moseley et al., 2016). As MCS in the Missouri River Valley occur when deep convection initiated in the Rocky Mountains in the late afternoon propagates eastwards, MCS frequency in St. Louis also presents interesting diurnal characteristics and dynamics. We decompose the monthly MCS frequency by hour of the day obtaining the frequencies

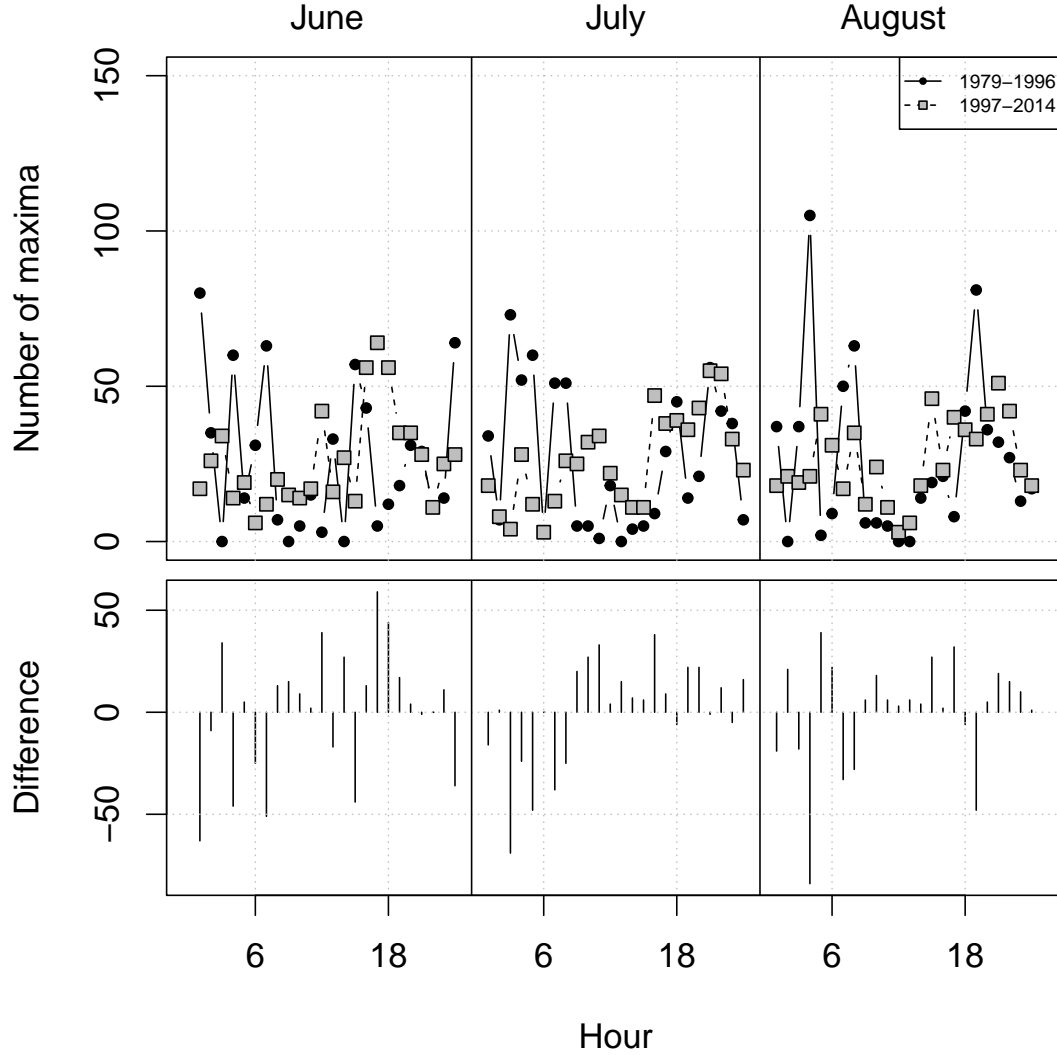
$$(1) \quad x_{t,h}^{(24)} = \frac{1}{D_t} \sum_{d=1}^{D_t} \tilde{x}_{hd}^t \quad \forall h \in \{1, \dots, 24\},$$

to capture these diurnal attributes. Figure 4 shows the average MCS frequency in Eq. (1) by hour  $h$  in June, July, and August when pooling across locations. Again, we show the averages for the 1979-1996 and 1997-2014 periods to highlight a possible shift. For June, the timing distribution of the MCS has not changed over time, but the MCS have become much more frequent: going from 0.005 at 9pm in 1979-1996 to 0.025 at 9pm in 1997-2014, a five-fold increase. For July and August, there are fewer MCS in the early morning over 1997-2014 than over 1979-1996. There has been no increase in MCS in the overnight hours for July. MCS have become more frequent over the rest of the day for July and August, but increases are less than those observed for June.

<sup>3</sup>Given the short time series, we did not seek an *optimal* breakpoint to maximize any increases as the near-even split suffices for motivation.

<sup>4</sup>Two-sample tests for the equality of proportions (1 am to noon) in 1979-1996 and 1997-2014, vs proportion in 1979-1996 greater than that in 1997-2014, show significant differences for all three months (p-value= 7.874e-06, 1.875e-14, and 9.423e-05, for June, July, and August, respectively).

Fig 2: **Timing of monthly maximum hourly precipitation.** Top panel: number of monthly maxima by hour during the 1979-1996 period (discs) and during the 1997-2014 period (squares) for June, July, and August. Bottom panel: number of maxima by hour in 1997-2014 minus number of maxima by hour in 1979-1996. Results are aggregated over the 35 pixel locations in Figure 1 for each month.

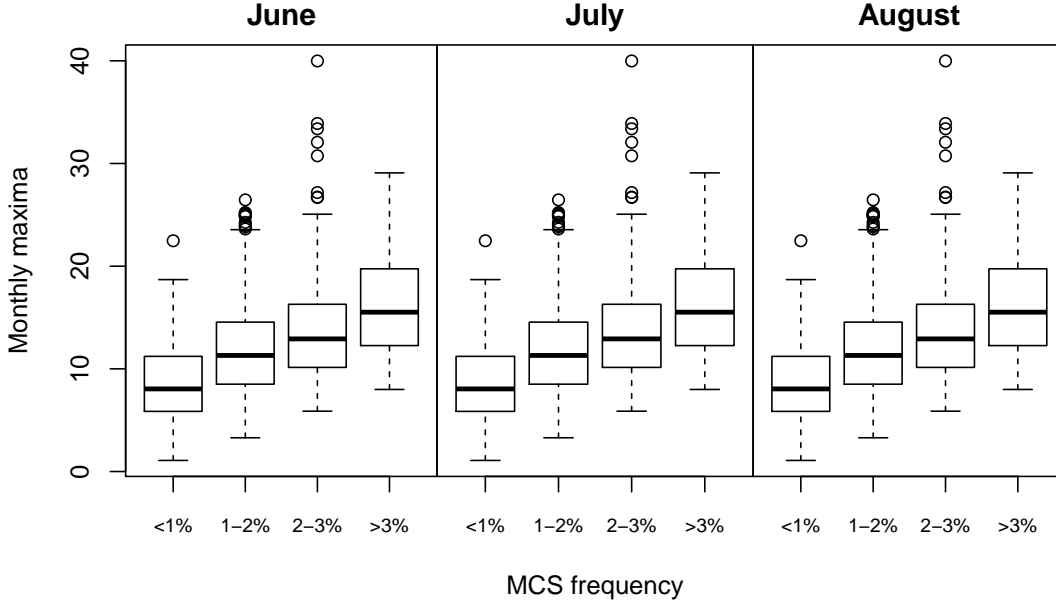


Given the strong diurnal pattern in both monthly maximum hourly rainfall and MCS frequency, we use linear <sup>5</sup> regression to explore whether their relationship also displays a diurnal pattern. The top panel of Figure 5 shows slope estimates from 24 linear regressions of monthly maximum hourly rainfall on the 12-hour centered average monthly MCS frequency (bottom panel), for the months of June, July, and August, pooling observations across locations. For June and August, all estimated coefficients are positive meaning that more frequent MCS lead to larger monthly maximum hourly rainfall, but no time-window is more impactful. A clear relationship is identified for July however: more frequent mid-afternoon MCS

<sup>5</sup>Data have large variability, but are quite linear.



Fig 3: **Size of maxima by MCS frequency.** Observations are aggregated over the 35 pixel locations in Figure 1 for each month.



have more than three times the effect of more frequent overnight MCS. The plot for July gives some intuition, but a proper analysis of these data must account for the extremal nature of monthly maximum hourly rainfall. We build models to capture the July effect in the next section.

**3. Mixed-frequency extreme value models.** In this section, we present a mixed-frequency extreme value model extending the *Block Maxima* approach for the statistical analysis of the extreme values.

**3.1. Extreme Value Theory.** Let  $\tilde{Y}_1, \dots, \tilde{Y}_n$  be a sample of *iid* observations drawn from a distribution function  $F$  and define the sample maxima  $Y_n = \max\{\tilde{Y}_1, \dots, \tilde{Y}_n\}$ . The extreme value theorem states that if there exist sequences of normalizing constants  $a_n$  and  $b_n$  such that the sample maxima converges to a non-degenerate limit,  $\frac{Y_n - a_n}{b_n} \xrightarrow{d} G(\cdot)$ , as  $n \rightarrow \infty$ , then  $G(\cdot)$  must be the extreme value distribution,

$$G(y) = \exp \left\{ -(1 + \xi y)^{-1/\xi} \right\}, \quad \xi \in \mathbb{R}, \quad 1 + \xi y > 0,$$

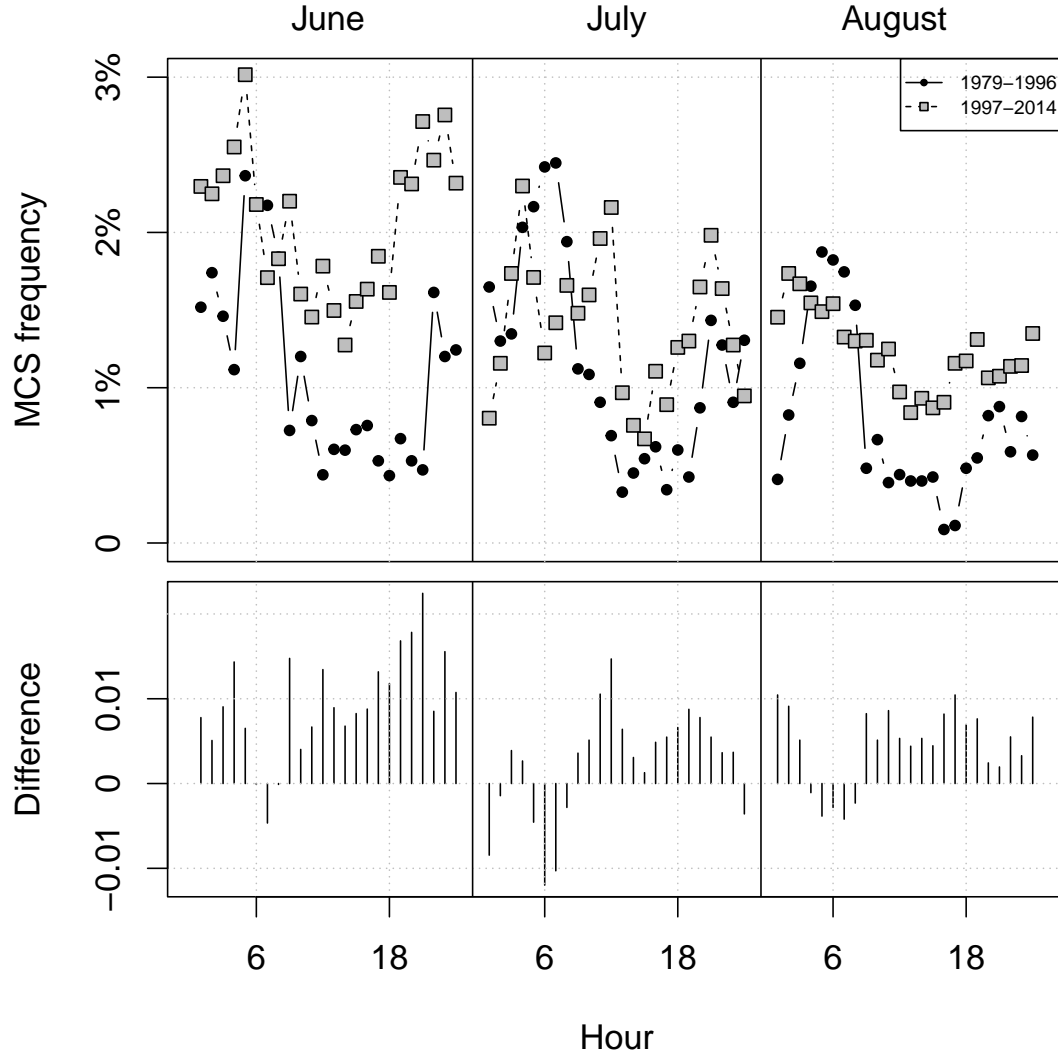
and  $F$  is said to be in the domain of attraction of the extreme value distribution. See Chapter 3 of [Embrechts, Klüppelberg and Mikosch \(1997\)](#) for a nice history of the theoretical contributions that lead to the above result.

This limiting result can be exploited to build an inference strategy on the maxima of a distribution. If a large sample of observations is available and these are independently drawn from the same distribution, then one can fit the Generalized Extreme Value (GEV) distribution,

$$H(y|\mu, \sigma, \xi) = \begin{cases} \exp \left\{ -(1 + \xi \frac{y - \mu}{\sigma})^{-1/\xi} \right\}, & 1 + \xi \frac{y - \mu}{\sigma} > 0 \quad \xi \neq 0 \\ \exp \left\{ -\exp(-\frac{y - \mu}{\sigma}) \right\}, & y \in \mathbb{R}, \quad \xi = 0 \end{cases}$$



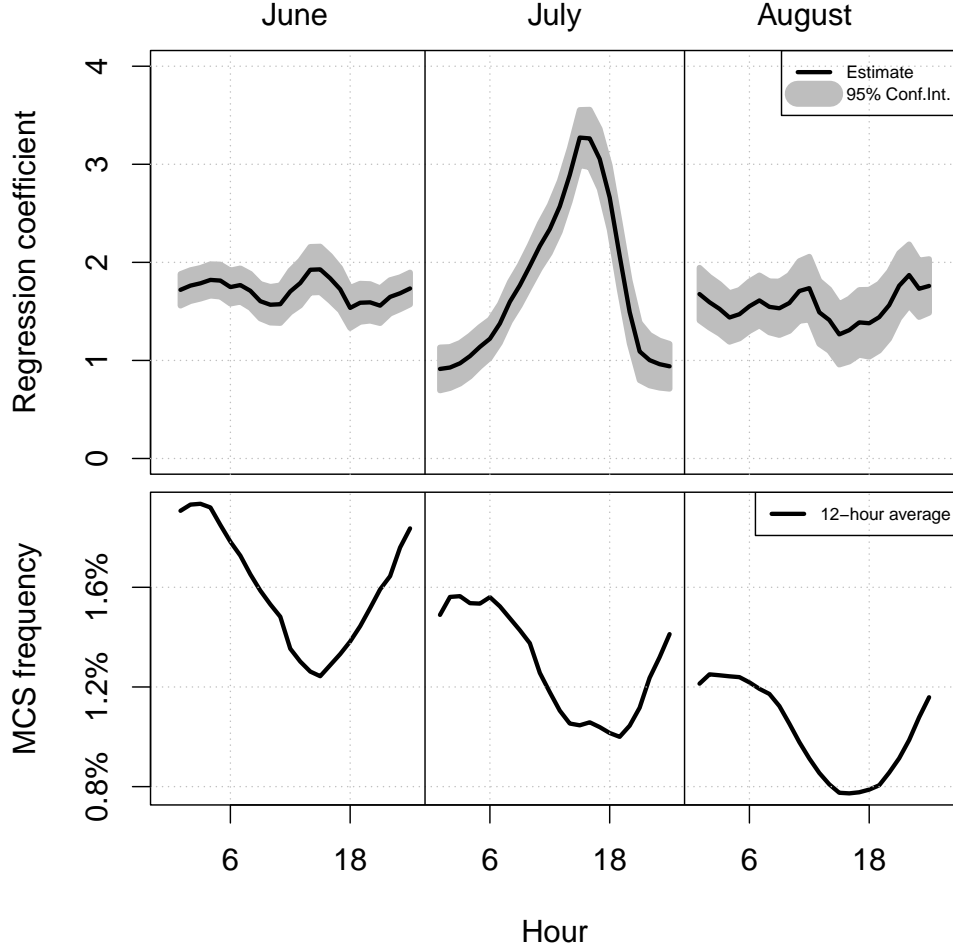
Fig 4: **Timing of MCS.** Top panel: average MCS frequency in Eq. (1), when pooling across the 35 pixel locations, by hour during the 1979-1996 period (discs) and during the 1997-2014 period (squares) for June, July, and August. Bottom panel: MCS frequency by hour in 1997-2014 minus average MCS frequency by hour in 1979-1996.



with  $\sigma > 0$  and  $\mu \in \mathbb{R}$  to maxima of subsamples. The  $\mu$ ,  $\sigma$ , and  $\xi$  are location, scale, and tail parameters, respectively. The GEV is also the only non-degenerate limit distribution for stationary series satisfying the  $D(U_n)$  condition (Leadbetter, 1974; Leadbetter, Lindgren and Rootzén, 1983). Use of the GEV for monthly maximum hourly rainfall is justified, as while hourly rainfall is not independent, it should follow the  $D(U_n)$  condition. See Coles (2001) and references therein for numerous published applications of the GEV model in many different disciplines.

**3.2. Mixed-Frequency GEV model.** No asymptotic theory can be established for non-stationary block maxima and the usual practice is to use the GEV model as a template and model the non-stationarity by allowing parameters to vary with time and other covariates.

Fig 5: **Possible diurnal pattern in impact of MCS.** Top panel: slope estimates (black line) and 95%-confidence intervals (gray cloud) from linear regressions of monthly maximum hourly rainfall on the 12-hour centered average monthly MCS frequency ( $\times 10^2$ ). Bottom panel: 12-hour centered average monthly MCS frequency.



This is the statistical approach followed here. Let  $Y_1, \dots, Y_m$  be a sequence of  $m$  block maxima with distribution  $\text{GEV}(y|\mu_t, \sigma_t, \xi_t)$ ,  $t \in \{1, \dots, m\}$ . In a standard extreme value regression setting, one would let the parameters  $(\mu_t, \sigma_t, \xi_t)$  vary according to vectors of block covariates  $\mathbf{x}_t$ , obtaining  $\mu_t = \mu(\mathbf{x}_t)$ ,  $\sigma_t = \sigma(\mathbf{x}_t)$  and  $\xi_t = \xi(\mathbf{x}_t)$ . Parametric and non-parametric functionals are available, and the relevant inferential strategies are well established in the literature (Beirlant et al., 2004). The maximum hourly rainfall is being retained over a *block of one month* and we have 24 MCS frequencies (1) per month, and so the covariate is sampled at a higher frequency than the maxima. Common practice suggests to conveniently aggregate (average) the data to obtain  $\mathbf{x}_t$ , however an arbitrary aggregation scheme may lead to an inefficient use of the covariate information. Given the diurnal pattern observed for July in Figure 5, the equal contribution implied by an average seems inappropriate. Any weighting should however be flexible and data-driven.

We consider a model where the location parameter  $\mu$  varies as a function of the MCS frequency by hour  $x_{t,h}^{(24)}$ ,  $h = 1, \dots, 24$ , defined in Eq. (1), and keep the scale parameter  $\sigma$  and shape parameter  $\xi$  constant. We let the block maxima  $Y_t$  follow a GEV distribution with

$Y_t | \mathbf{x}_t^{(24)} \sim H(y | \mathbf{x}_t^{(24)}, \boldsymbol{\theta})$  with

$$(2) \quad \mu_t = \kappa_0 + \kappa_1 \mathbf{w}(\phi) \cdot \mathbf{x}_t^{(24)}$$

where  $\mathbf{x}_t^{(24)} = (x_{t,1}^{(24)}, \dots, x_{t,24}^{(24)})' \in \mathbb{R}^{24}$ ,  $\mathbf{w}(\phi) = (w(1|\phi), \dots, w(24|\phi))' \in \mathbb{R}^{24}$  is a vector of weights obtained from a parametric weighting function  $w(\cdot|\phi) \in (0, 1)$  such that  $\|\mathbf{w}(\phi)\|_1 = 1$ ,  $\cdot$  denotes the dot product, and  $\boldsymbol{\theta} = (\kappa, \sigma, \xi, \phi) \in \mathbb{R}^{28}$  is a vector of parameters. The latter model is a special case of our Mixed-Frequency GEV (MFGEV) model detailed in Appendix B. The motivation behind this approach is that of optimally aggregating the  $q = 24$  observations of the MCS covariate in the  $t$ th block according to a weighting scheme that is obtained from a function  $w(\cdot|\phi)$  whose parameter  $\phi$  needs to be estimated from the data. Using a well-known adage in the extreme value literature, we are further *letting the tails speak for themselves*. Other low-frequency ( $q = 1$ ) covariates can be added to Eq. (2) to model any additional non-stationarity. These covariates will be discussed in Section 4 and are omitted here to keep notation simple.

The weighting function has to be specified by the researcher. When  $w(\cdot|\phi) = 1/q$ , we are back to the simple averaging scheme. In our analysis, we rely on the *Beta* weighting function

$$(3) \quad w(r|\phi) = \frac{\beta\left(\frac{r}{q}|\phi, \phi\right)}{\sum_{r=1}^q \beta\left(\frac{r}{q}|\phi, \phi\right)}, \quad \phi \in \mathbb{R}_+$$

where  $\beta(z|a, b) = z^{a-1}(1-z)^{b-1} / \int_0^1 u^{a-1}(1-u)^{b-1} du$  is the probability density function of a Beta distribution. Figure 6 shows the values of the Beta weighting function for four different values of  $\phi$  and can be interpreted as follows. If  $r = 1$  represents 1 am when  $q = 24$  hours,  $\phi < 0$  ( $> 0$ ) corresponds to more weight to late night (late morning) and late evening (early afternoon) hours. Changing the hour corresponding to  $r = 1$  adds further flexibility to the distribution of the weights across the hours of the day. The Beta weighing function must be restrained in some way to have identification (Ghysels and Qian, 2019) and our one-parameter specification allows for the inverted U-shape behavior seen in the exploratory analysis in Figure 5.

**3.3. Inference.** Estimation of model parameters in (2) (and (7)) can be performed at each pixel location using Maximum Likelihood. We instead pool observations across locations, improving efficiency and increasing testing power compared to the estimation at a single location. The idea is similar to that of regionalization methods in hydrology (Asadi, Engelke and Davison, 2018): we exploit the information at all  $l = 35$  locations without modeling the joint dependence structure. Pooling data from 35 locations, over a less than 100 km x 100 km grid, with elevations of mean  $\approx 154$  m and standard deviation  $\approx 24$  m, enables better parameter estimation without introducing too much noise.

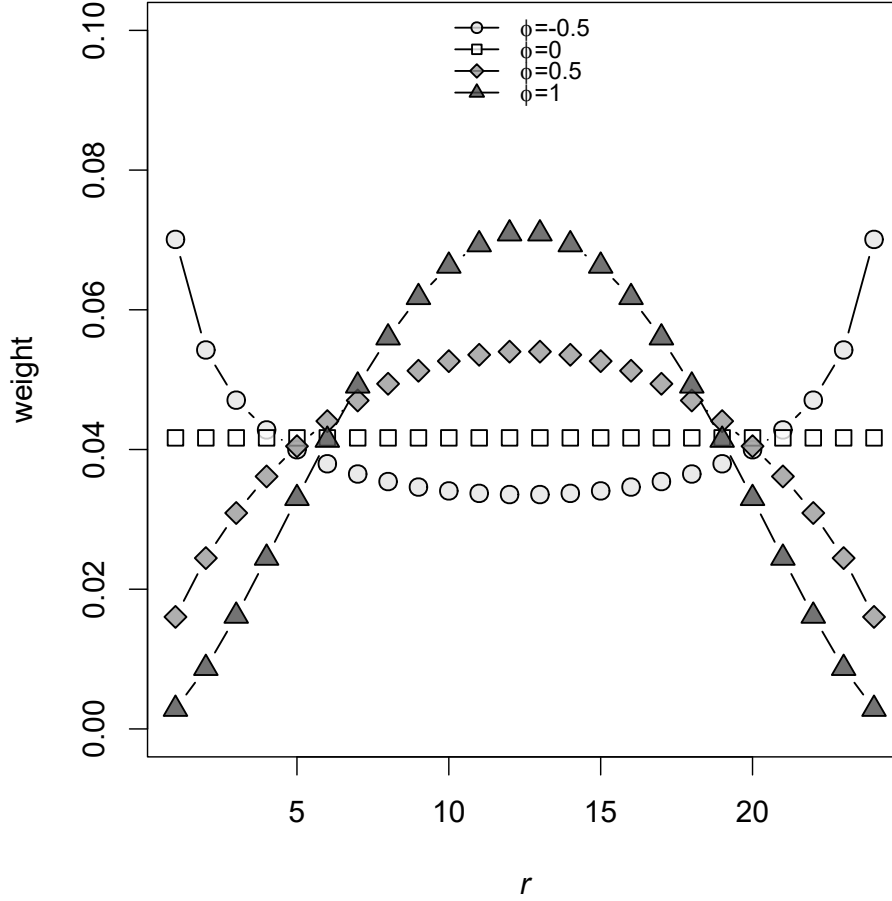
Let  $Y_{i,t}$  and  $\mathbf{x}_{i,t}^{(24)}$  be the maxima and the MCS covariate from the  $t$ th block at the  $i$ th location, respectively, with  $t \in \{1, \dots, m\}$  and  $i \in \{1, \dots, l\}$ . At each location in the homogeneous area, we define the pooled MFGEV model as  $Y_{i,t} \sim H(y; \mathbf{x}_{i,t}^{(24)} | \boldsymbol{\theta})$  with shape parameter  $\xi$ , scale parameter  $\sigma$ , and location

$$(4) \quad \mu_{i,t} = \kappa_0 + \kappa_1 \mathbf{w}(\phi) \cdot \mathbf{x}_{i,t}^{(24)}$$

where  $\boldsymbol{\theta} = (\kappa, \sigma, \xi, \phi)$  gathers the common slope and weighting parameters. We use Quasi Maximum Likelihood (QML) to estimate  $\boldsymbol{\theta}$ , i.e.

$$(5) \quad \hat{\boldsymbol{\theta}}_{\text{QML}} := \underset{\boldsymbol{\theta}}{\operatorname{argmax}} \sum_{t=1}^m \sum_{i=1}^l \log h(y_{it}; \mathbf{x}_{i,t}^{(24)} | \boldsymbol{\theta})$$

Fig 6: **Beta weighting function.** Four specifications of the Beta weighting function in Eq. (3) for  $r = 1, \dots, q$  and  $q = 24$ .



with  $h(y; x|\theta)$  the density of the GEV distribution,

$$h(y; x|\theta) = \frac{1}{\sigma} \left( 1 + \xi \frac{y - \mu(x; \theta)}{\sigma} \right)^{-1 - \frac{1}{\xi}} \exp \left( 1 + \xi \frac{y - \mu(x; \theta)}{\sigma} \right)^{-\frac{1}{\xi}}.$$

The QML estimator maximizes an independent likelihood despite the presence of spatial dependence among the locations. This approach yields consistent and asymptotically normal estimates though it can lose efficiency (Chandler and Bate, 2007). The alternative would be to perform ML estimation using a max-stable dependence model, but since our interest is in the marginals, the simpler QML is preferred as it avoids problems related to assuming the wrong dependence structure. To account for the possible spatial dependence, inference on the model parameters is performed using a stratified bootstrap as in Asadi, Engelke and Davison (2018): (i) We partition the years in the sample into  $S = 3$  strata; (ii) for each stratum, we resample  $B$  times with equal probability and replacement from the months in the stratum, thus preserving any spatial dependence among the different locations; (iii) we estimate the pooled MFGEV model on the  $B$  bootstrap datasets and obtain  $(1 - \alpha)$  confidence intervals for the model parameters computing  $\alpha/2$  and  $(1 - \alpha/2)$  quantiles of the bootstrap estimates.

A simulation study in Appendix C confirms that the QML estimator performs well and that the bootstrapped confidence intervals allow for a reliable inference. Functions to carry out all the computations are written in an R package available upon request.

**4. Empirical Analysis.** The exploratory data analysis in Figure 5 suggests that MCS frequency in different parts of the day may not contribute evenly to explain extreme hourly rainfall intensity during the month of July. The MFGEV model developed in Section 3.2 is suitable to capture such diurnal effects. We fit the MFGEV model in (4) where  $w(\phi)$  is the Beta weighting function in (3) to monthly maximum hourly rainfall for the month of July. Formally, let  $Y_{i,t}$  denote the monthly maximum hourly precipitation in July from the  $t$ th year at the  $i$ th location and let  $\mathbf{x}_{\text{MCS},i,t}^{(24)}$  be the corresponding vector of 24 hourly MCS frequencies. We consider the pooled model  $Y_{i,t} \sim H(y; \mu(\mathbf{x}_{\text{MCS},i,t}^{(24)}, t, x_{\text{Temp},t}, x_{\text{SOI},t}, x_{\text{PDO},t}), \sigma, \xi)$  with

$$(6) \quad \mu_{i,t} = \kappa_0 + \kappa_{\text{MCS}} \mathbf{w}(\phi_{\text{MCS}}) \cdot \mathbf{x}_{\text{MCS},i,t}^{(24)} + \kappa_{\text{Trend}} t + \kappa_{\text{Temp}} x_{\text{Temp},t} + \kappa_{\text{SOI}} x_{\text{SOI},t} + \kappa_{\text{PDO}} x_{\text{PDO},t}$$

where  $i = 1, \dots, 35$ ,  $t = 1, \dots, 36$ ,  $w(\cdot|\phi_{\text{MCS}})$  is the Beta weighting function (3) with  $q = 24$  hours. Besides the MCS frequency, we include a time trend and the explanatory variables discussed in Section 1, obtaining the data from NOAA: temperature<sup>6</sup>, SOI<sup>7</sup>, and PDO<sup>8</sup>. Temperature data are monthly mean temperature at St Louis Lambert International Airport. We include all the *usual* covariates to guard against estimated MCS effects being the result of unmodeled non-stationarity. We fit five specifications for  $\mu_{i,t}$ : Eq.(6) and four subset models. Models that also include the covariates in the scale parameter  $\sigma$  were considered, but they yielded non-significant parameter estimates, so they are not reported.

An additional modeling issue is the correspondence between the value of  $r$  in (3) and the hour of the day. We consider all possibilities. We let  $r = 1$  represent each of the 24 possible hours and retain the setting that maximizes the likelihood. For our five model specifications, the likelihood is maximized when  $r = 1$  corresponds to 2 am. Table 1 shows the parameter estimates under this setting. Parameter estimates of  $\kappa_{\text{MCS}}$ ,  $\phi_{\text{MCS}}$ ,  $\gamma$  and  $\xi$  are stable across the five specifications. Parameter estimates for  $\kappa_{\text{MCS}}$  are always positive and statistically significant, confirming that the MCS rate is a strong predictor of the monthly maximum hourly precipitation. Confidence interval estimates for non-MCS parameters never indicate significant effects. Point estimates of the time trend parameter are positive, but the bootstrap confidence intervals suggest a non-significant effect. For all five specifications, point estimates for  $\phi_{\text{MCS}}$  are roughly equal to 1, a value of  $\phi$  which corresponds to considerably more weight on MCS hourly frequencies near 1pm and 2 pm given  $r = 1$  is set to 2 am (recall shapes of the Beta weighting function in Figure 6). Figure 7 shows the point and confidence interval estimates of the weights for all five specifications. The dark gray cloud exceeds the black curve (uniform weight) in the afternoon and is below the black curve in the overnight hours. The 1-2 pm peak is a few hours earlier than in the diurnal pattern detected in the exploratory data analysis in Figure 5, but these empirical Beta weights are computed within an appropriate likelihood function where the extremal nature of monthly maxima is considered and the covariate has not been smoothed. Finally, estimates of  $\xi$  are always positive though the confidence intervals suggest they are never significantly different from zero. This does not necessarily imply that maximum hourly precipitation is not heavy tailed as we are modeling heterogeneity with Eq. (6), see Einmahl and He (2022).

<sup>6</sup><https://www.ncdc.noaa.gov/cdo-web/search>

<sup>7</sup><https://www.ncdc.noaa.gov/teleconnections/enso/indicators/soi/data.csv>

<sup>8</sup><https://www.ncdc.noaa.gov/teleconnections/pdo/data.csv>

To better appreciate the impact of heterogeneous weights across the hours of the day, we compare specification (i) in Table 1 with an alternative where weights are constrained to be uniform, i.e.  $\phi_{\text{MCS}} = 0$ . For both models, we compute the 99th quantile at each location under three scenarios:

- (a) the MCS frequency equals the in-sample average across the years;
- (b) the MCS frequency is twice as large as the MCS frequency in scenario (a);
- (c) the MCS frequency is twice as large as the MCS frequency in scenario (a) on average, but grows more during daytime hours following an inverted U-shaped pattern to mimic changes seen in the bottom panel of Figure 4 for July.

Finally, we take scenario (a) as the reference and compute the growth rates in the quantiles of both models under scenarios (b) and (c). We find that the average growth rate across locations is 29% and 34% under scenario (b), and 29% and 39% under scenario (c), for the model with uniform and beta weights, respectively. Letting the weights to vary across the hours of the day can have a large impact on upper quantiles.

To assess the goodness of fit of our MFGEV model, we perform a graphical validation using a QQ-plot (Beirlant et al., 2004). We use the transformation

$$R_{i,t} = \frac{1}{\hat{\xi}} \log \left( 1 + \hat{\xi} \frac{\hat{Y}_{i,t} - \hat{\mu}_{i,t}}{\hat{\sigma}} \right)$$

to obtain Gumbel random variables that no longer depend on the covariates. We can thus compare the quantiles of  $R_1, \dots, R_n$  against the Gumbel quantiles. Figure 8 shows the QQ-plot at each pixel location for the fitted MFGEV model with specification (i). The fits are generally satisfactory, most observations lying well within confidence bounds, though in a few locations the model seems to underestimate the tail probabilities. This might be due to the pooling of observations, but it could also just be a small sample effect associated to the short time series. To investigate this possibility, we count the number of times the sample maximum exceeds the model-implied 90th quantile at each location and find that the observed number of violations is comparable to that obtained in a unreported simulation using the estimated model as the data generating process.

We also use the  $R_{i,t}$  to check for any spatial dependence remaining in the residuals after conditioning on the MCS covariates. We find that the pairwise correlation among locations is on average 0.39 (st.dev. 0.25) and that the pairwise tail dependence computed at the 90th quantile is on average 0.34 (st.dev. 0.26). The simulation study in Appendix C suggests that such dependence does not affect the size of the hypothesis test of flat weights ( $\phi = 0$ ), but can reduce its power. This implies that our significance results on the weighting parameter  $\phi$  are somewhat conservative.

**5. Discussion.** Westra et al. (2014) call for more thorough observational and modeling studies exploring the dominant processes that could further drive extreme rainfall in a future climate, and a more recent similar appeal appears in Fowler, Wasko and Prein (2021). We develop a mixed-frequency extreme value model that allows for a flexible integration of covariates observed at a higher frequency than the sample maxima. We use this novel framework to gain a better understanding of how changes to MCS frequency have affected extreme rainfall intensities as measured by monthly maximum hourly rainfall.

Examination of records from the greater St.Louis area shows that MCS frequency has a strong positive impact on hourly extreme rainfall intensity, but this impact is not necessarily uniform over the day. We document an important diurnal pattern in the way MCS frequency affects monthly maximum hourly precipitation levels in July. Figure 5 shows a middle-day hump for the impact of MCS frequency on monthly maxima and Figure 7 shows that our

TABLE 1

**Fitted MFGEV models.** Point estimates and 95% bootstrap confidence intervals for five specifications (Spec) including: the monthly MCS occurrence rate (MCS), a trend component (Trend), the monthly average temperature (Temp), and the monthly value of Southern Oscillation Index (SOI) and Pacific Decadal Oscillation (PDO). Confidence intervals are computed using  $B = 500$  bootstrap samples.

Spec.	$\kappa_{\text{MCS}}$	$\kappa_{\text{Trend}}$	$\kappa_{\text{Temp}}$	$\kappa_{\text{SOI}}$	$\kappa_{\text{PDO}}$	$\phi_{\text{MCS}}$	$\gamma$	$\xi$
(i)	2.47 (1.94; 3.37)					1.01 (0.47; 1.49)	1.21 (1.06; 1.33)	0.08 (-0.01; 0.17)
(ii)	2.45 (1.85; 3.22)	0.037 (-0.01; 0.11)				0.96 (0.54; 1.52)	1.21 (1.05; 1.32)	0.07 (-0.02; 0.16)
(iii)	2.44 (1.89; 3.30)		-0.036 (-0.27; 0.30)			1.01 (0.57; 1.56)	1.21 (1.05; 1.32)	0.08 (-0.01; 0.18)
(iv)	2.43 (1.82; 3.24)	0.036 (-0.013; 0.11)	-0.029 (-0.25; 0.36)			0.97 (0.49; 2.81)	1.21 (1.06; 1.29)	0.07 (-0.02; 0.16)
(v)	2.47 (1.68; 3.21)	0.031 (-0.052; 0.11)	-0.04 (-0.32; 0.36)	-0.47 (-1.20; 0.56)	-0.05 (-0.27; 0.67)	0.97 (0.33; 2.21)	1.20 (1.02; 1.29)	0.08 (-0.03; 0.16)

model successfully captures and estimates this behavior. Climate models need to reproduce this characteristic. The importance of the latter is amplified by the uneven diurnal increases in MCS frequency over time observed in Figure 4 and the forecast that MCS frequency could more than triple in North America by the end of the 21st century (Prein et al., 2017). CPM simulations not able to reproduce these characteristics in the data will continue to underestimate extreme hourly precipitation in the region.

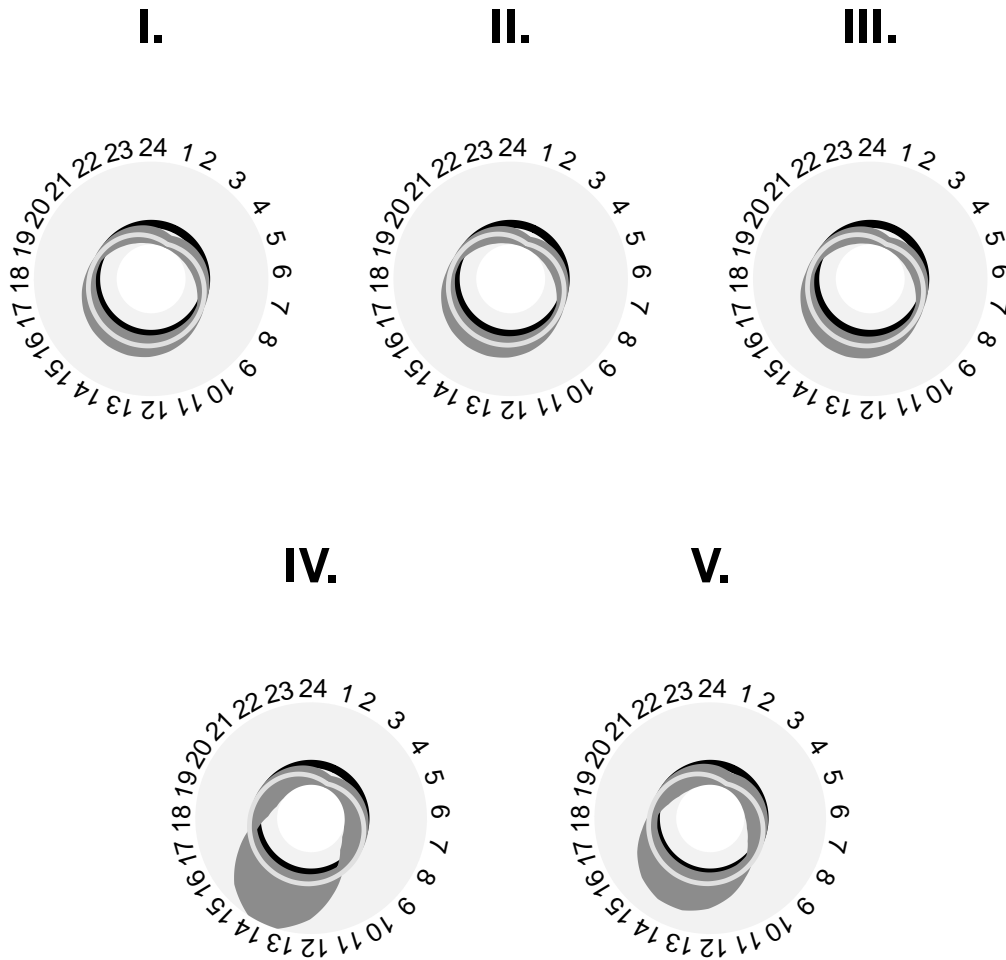
Our study of St. Louis in July is compelling and our discovery of previously undocumented empirical findings is perhaps not surprising given the CPMs' inability to reproduce MCS characteristics in the area (see Section 1). The feature-based evaluation presented in Prein et al. (2020) allows some individual components of the bias to be identified. Our model could also be exploited to check that observed relationships are borne out by CPM simulated data. Our maximum hourly rainfall problem is set within the block maxima setting to directly estimate the more infrequent events required for engineering design, but our mixed frequency block maxima models can be adapted to threshold exceedances. For instance, one might be interested in tying daily exceedances to covariates sampled at an intra-day frequency, see Bee, Dupuis and Trapin (2019) for a financial application.

## REFERENCES

- AHMADALIPOUR, A. and MORADKHANI, H. (2019). A data-driven analysis of flash flood hazard, fatalities, and damages over the CONUS during 1996-2017. *Journal of Hydrology* **578**. <https://doi.org/10.1016/j.jhydrol.2019.124106>.
- ALMUKHTAR, S., MIGLIOZZI, B., SCHWARTZ, J. and WILLIAMS, J. (2019). The Great Flood of 2019: A Complete Picture of a Slow-Motion Disaster. <https://www.nytimes.com/interactive/2019/09/11/us/midwest-flooding.html>.
- ASADI, P., ENGELKE, S. and DAVISON, A. C. (2018). Optimal regionalization of extreme value distributions for flood estimation. *Journal of Hydrology* **556** 182–193. <https://doi.org/10.1016/j.jhydrol.2017.10.051>.
- ASHLEY, S. T. and ASHLEY, W. S. (2008). Flood fatalities in the United States. *Journal of Applied Meteorology and Climatology* **47** 805–818.
- BARBERO, R., FOWLER, H. J., LENDERINK, G. and BLENKINSOP, S. (2017). Is the intensification of precipitation extremes with global warming better detected at hourly than daily resolutions? *Geophysical Research Letters* **44** 974–983.
- BARBERO, R., FOWLER, H. J., BLENKINSOP, S., WESTRA, S., MORON, V., LEWIS, E., CHAN, S., LENDERINK, G., KENDON, E., GUERREIRO, S., LI, X., VILLALOBOS, R., ALI, H., and MISHRA, V. (2019). A synthesis of hourly and daily precipitation extremes in different climatic regions. *Weather and Climate Extremes* **26**. <https://doi.org/10.1016/j.wace.2019.100219>.
- BEE, M., DUPUIS, D. J. and TRAPIN, L. (2019). Realized peaks over threshold: a time-varying extreme value approach with high-frequency based measures. *Journal of Financial Econometrics* **19** 254–283.

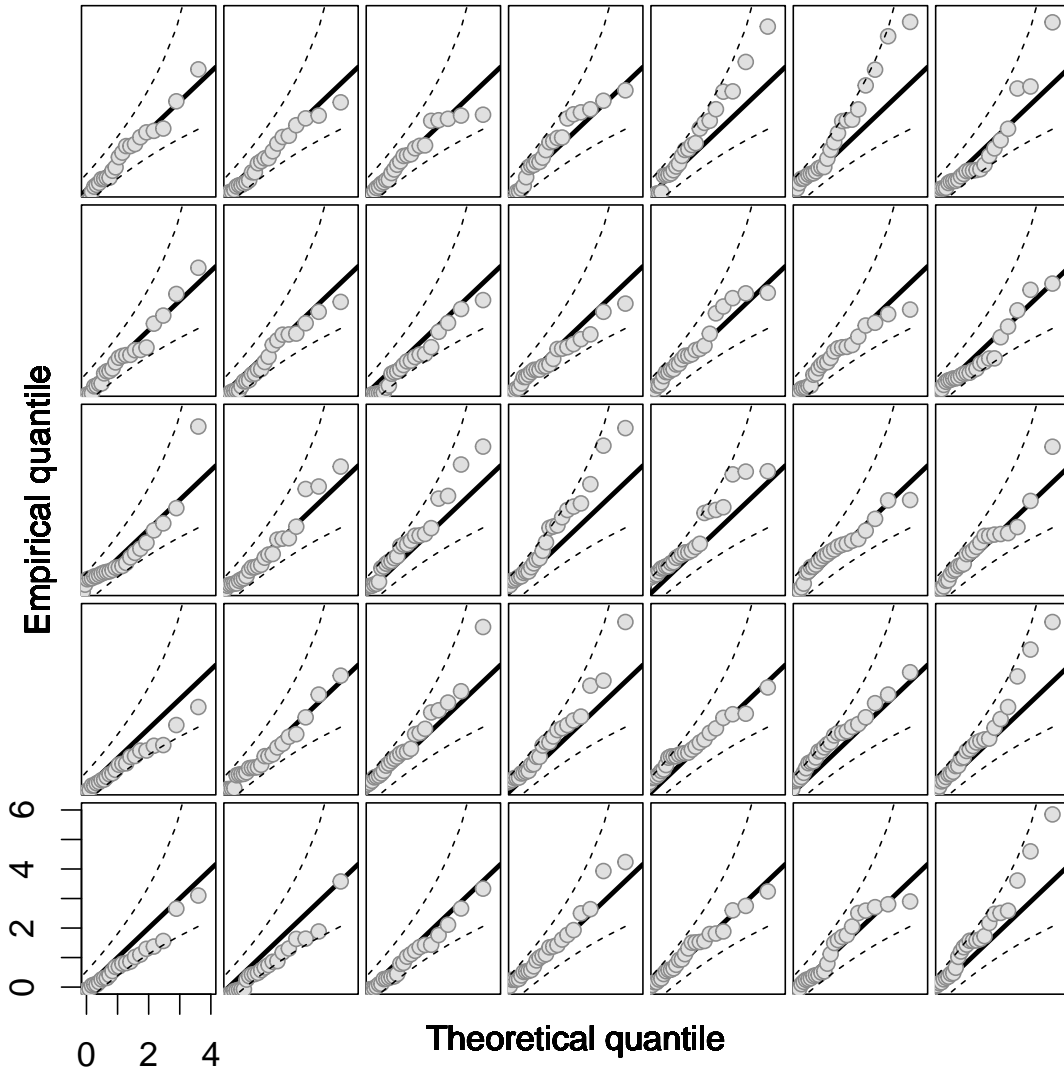


Fig 7: **Estimated Beta weights.** Point estimates of Beta weights (white line), Beta weight bounds implied by the 95% confidence interval (dark gray cloud), and uniform weights (black line). The light-gray-shaded area spans values from 0 (inner rim) to 0.2 (outer rim). Weights are for the 24 hours of the day as shown on the most outer rim.



- BEIRLANT, J., GOEGEBEUR, Y., SEGERS, J. and TEUGELS, J. L. (2004). *Statistics of Extremes: Theory and Applications*. John Wiley & Sons.
- CALLAU PODUJE, A. C. and HABERLANDT, U. (2017). Short time step continuous rainfall modeling and simulation of extreme events. *Journal of Hydrology* **552** 182–197.
- CARBONE, R. E. and TUTTLE, J. D. (2008). Rainfall occurrence in the U.S. warm season: the diurnal cycle. *Journal of Climate* **21** 4132–4146.
- CARREAU, J. and TOULEMONDE, G. (2020). Extra-parametrized extreme value copula: Extension to a spatial framework. *Spatial Statistics*. <https://doi.org/10.1016/j.spasta.2020.100410>.
- CHANDLER, R. E. and BATE, S. (2007). Inference for clustered data using the independence loglikelihood. *Biometrika* **94** 167–183.
- COLES, S. (2001). *An Introduction to Statistical Modeling of Extreme Values*. Springer.

Fig 8: **Goodness of fit.** QQ-plots at 35 pixel locations in Figure 1 for fitted MFGEV model with specification (i) (see Table 1). Plots are on a common Gumbel scale. Dotted lines show bounds of 95% confidence intervals based on the distribution of order statistics.



DAI, A. and TRENBERTH, K. (2004). The diurnal cycle and its depiction in the community climate system model. *Journal of Climate* **17** 930–951. [https://doi.org/10.1175/1520-0442\(2004\)017<0930:TDCAID>2.0.CO;2](https://doi.org/10.1175/1520-0442(2004)017<0930:TDCAID>2.0.CO;2).

DAVIES, R. (2014a). Federal Aid for Missouri September Floods. <https://floodlist.com/dealing-with-floods/federal-aid-missouri-september-floods>.

DAVIES, R. (2014b). Storms Hit Central USA - Floods in Missouri, Illinois and Iowa. <https://floodlist.com/america/usa/storms-hit-central-usa-floods-missouri-illinois-iowa>.

DAVIES, R. (2017). USA - Flash Floods in New Orleans, Kansas City and Las Vegas. <https://floodlist.com/america/usa/usa-flash-floods-in-new-orleans-kansas-city-and-las-vegas>.

EINMAHL, J. H. J. and HE, Y. (2022). Extreme Value Estimation for Heterogeneous Data. *Journal of Business & Economic Statistics*. doi:10.1080/07350015.2021.2008408.

- EMBRECHTS, P., KLÜPPELBERG, C. and MIKOSCH, T. (1997). *Modelling Extremal Events: for Insurance and Finance* **33**. Springer Science & Business Media.
- EVANS, J. and WESTRA, S. (2012). Investigating the mechanisms of diurnal rainfall variability using a regional climate model. *Journal of Climate* **25** 7232–7247. <https://doi.org/10.1175/JCLI-D-11-00616.1>.
- FENG, Z., LEUNG, L. R., HAGOS, S., HOUZE, R. A., BURLEYSON, C. D. and BALAGURU, K. (2016). More frequent intense and long-lived storms dominate the springtime trend in central US rainfall. *Nature Communications* **7** 13429.
- FENG, Z., SONG, F., SAKAGUCHI, K. and LEUNG, L. R. (2021). Evaluation of Mesoscale Convective Systems in Climate Simulations: Methodological Development and Results from MPAS-CAM over the United States. *Journal of Climate* **34** 2611–2633.
- FOWLER, H. J., WASKO, C. and PREIN, A. F. (2021). Intensification of short-duration rainfall extremes and implications for flood risk: current state of the art and future directions. *Phil. Trans. R. Soc. A* **379**. <https://doi.org/10.1098/rsta.2019.0541>.
- GHYSELS, E. and QIAN, H. (2019). Estimating MIDAS regressions via OLS with polynomial parameter profiling. *Econometrics and Statistics* **9** 1–16.
- GOURLEY, J., HONG, Y., FLAMIG, Z., LI, L. and WANG, J. (2017). The FLASH Project: Improving the tools for flash flood monitoring and prediction across the United States. *Bull. Amer. Meteor. Soc* **98** 361–372.
- KENDON, E. J., BLENKINSOP, S. and FOWLER, H. J. (2018). When will we detect changes in short-duration precipitation extremes? *Journal of Climate* **31** 2945–2964.
- KOUTSOYIANNIS, D., KOZONIS, D. and MANETAS, A. (1998). A mathematical framework for studying rainfall intensity-duration-frequency relationships. *Journal of Hydrology* **206** 118–135.
- KUNKEL, K. E., KARL, T. R., BROOKS, H., KOSSIN, J., LAWRIKMORE, J. H., ARNDT, D., BOSART, L., CHANGNON, D., CUTTER, S. L., DOESKEN, N. et al. (2013). Monitoring and understanding trends in extreme storms: state of knowledge. *Bulletin of the American Meteorological Society* **94** 499–514.
- LARSON, L. W. (1996). The Great USA Flood of 1993. [https://www.nwrfc.noaa.gov/floods/papers/oh\\_2/great.htm](https://www.nwrfc.noaa.gov/floods/papers/oh_2/great.htm).
- LEADBETTER, M. R. (1974). On extreme values in stationary sequences. *Z. Wahrsch. Verw. Gebiete* **28** 289–303.
- LEADBETTER, M. R., LINDGREN, G. and ROOTZÉN, H. (1983). *Extremes and Related Properties of Random Sequences and Processes*. Springer.
- LI, J. (2017). Hourly station-based precipitation characteristics over the Tibetan Plateau. *International Journal of Climatology*. <https://doi.org/10.1002/joc.5281>.
- MASSONDELMOTTE, V., ZHAI, P., PIRANI, A., CONNORS, S. L., PÉAN, C., BERGER, S., CAUD, N., CHEN, Y., GOLDFARB, L., GOMIS, M. I., HUANG, M., LEITZELL, K., LONNOY, E., MATTHEWS, J. B. R., MAYCOCK, T. K., WATERFIELD, T., YELEKÇI, O., YU, R. and (EDS. ), B. Z. (2021). IPCC, 2021: Summary for Policymakers. In: *Climate Change 2021: The Physical Science Basis. Contribution of Working Group I to the Sixth Assessment Report of the Intergovernmental Panel on Climate Change*.
- MORON, V., BARBERO, R., EVANS, J., WESTRA, S. and FOWLER, H. (2019). Weather types and hourly to multi-day rainfall characteristics in Tropical Australia. *Journal of Climate* **32**. <https://doi.org/10.1175/JCLI-D-18-0384.1>.
- MOSELEY, C., HOHENEGGER, C., BERG, P. and HAERTER, J. O. (2016). Intensification of convective extremes driven by cloud-cloud interaction. *Nature Geoscience* **9**. <https://doi.org/10.1038/NGEO2789>.
- NESBITT, S. W., CIFELLI, R. and RUTLEDGE, S. A. (2006). Storm morphology and rainfall characteristics of TRMM precipitation features. *Monthly Weather Review* **134** 2702–2721. <https://doi.org/10.1175/Mwr3200.1>.
- NEWS, F. (2018). USA - Deadly Flash Floods in Kentucky and Missouri. <https://floodlist.com/america/usa/floods-storm-gordon-kentucky-missouri-september-2018>.
- O’GORMAN, P. A. (2012). Sensitivity of tropical precipitation extremes to climate change. *Nature Geosciences* **5** 697–700.
- OUARDA, T., YOUSEF, L. and CHARRON, C. (2019). Non-stationary intensity-duration-frequency curves integrating information concerning teleconnections and climate change. *International Journal of Climatology* **39**. <https://doi.org/10.1002/joc.5953>.
- PIELKE JR, R. A. and DOWNTON, M. W. (2000). Precipitation and damaging floods: trends in the United States, 1932–97. *Journal of Climate* **13** 3625–3637.
- PLOSHAY, J. and LAU, N. (2010). Simulation of the diurnal cycle in tropical rainfall and circulation during boreal summer with a high-resolution GCM. *Monthly Weather Review* **138** 3434–3453. <https://doi.org/10.1175/2010MWR3291.1>.
- PREIN, A. F., LIU, C., IKEDA, K., TRIER, S. B., RASMUSSEN, R. M., HOLLAND, G. J. and CLARK, M. P. (2017). Increased rainfall volume from future convective storms in the US. *Nature Climate Change* **7** 880.

- PREIN, A. F., LIU, C., IKEDA, K., BULLOCK, R., RASMUSSEN, R. M., HOLLAND, G. J. and CLARK, M. (2020). Simulating North American mesoscale convective systems with a convection-permitting climate model. *Climate Dynamics* **55** 95–110.
- SAHARIA, M., KIRSTETTER, P., VERGARA, H., GOURLEY, J., HONG, Y. and GIROUD, M. (2017). Mapping Flash Flood Severity in the United States. *Journal of Hydrometeorology* **18** 397–411.
- SEBILLE, Q., FOUGÈRES, A. L. and MERCADIER, C. (2017). Modeling extreme rainfall A comparative study of spatial extreme value models. *Spatial Statistics* **21** 187–208. <http://dx.doi.org/10.1016/j.spasta.2017.06.009>.
- SERVICE, N. W. (2022). Flash floods and floods...the Awesome Power! last consulted April 12, 2022. <https://www.weather.gov/pbz/floods>.
- STEVENSON, S. N. and SCHUMACHER, R. S. (2014). A 10-year survey of extreme rainfall events in the central and eastern United States using gridded multisensor precipitation analyses. *Monthly Weather Review* **142** 3147–3162. <https://doi.org/10.1175/MWR-D-13-00345.1>.
- TRENBERTH, K. E., DAI, A., RASMUSSEN, R. M. and PARSONS, D. B. (2003). The changing character of precipitation. *Bulletin of the American Meteorological Society* **84** 1205–1217.
- TYE, M. R. and COOLEY, D. (2015). A spatial model to examine rainfall extremes in Colorado’s Front Range. *Journal of Hydrology* **530** 15–23. <http://dx.doi.org/10.1016/j.jhydrol.2015.09.023>.
- WESTRA, S., FOWLER, H., EVANS, J., ALEXANDER, L., BERG, P., JOHNSON, F., KENDON, E., LENDERINK, G. and ROBERTS, N. (2014). Future changes to the intensity and frequency of short-duration extreme rainfall. *Reviews of Geophysics* **52** 522–555.
- ZHU, L., LIU, X. and LUND, R. (2019). A likelihood for correlated extreme series. *Environmetrics* **30**. <https://doi.org/10.1002/env.2546>.

## APPENDIX A: DATASET

TABLE 2  
*St. Louis Data Locations* Latitude and longitude of the 35 pixel locations in Figure 1.

lat.	long.	lat.	long.	lat.	long.	lat.	long.	lat.	long.
38.313	-90.563	38.438	-90.563	38.563	-90.563	38.688	-90.563	38.813	-90.563
38.313	-90.438	38.438	-90.438	38.563	-90.438	38.688	-90.438	38.813	-90.438
38.313	-90.313	38.438	-90.313	38.563	-90.313	38.688	-90.313	38.813	-90.313
38.313	-90.188	38.438	-90.188	38.563	-90.188	38.688	-90.188	38.813	-90.188
38.313	-90.063	38.438	-90.063	38.563	-90.063	38.688	-90.063	38.813	-90.063
38.313	-89.938	38.438	-89.938	38.563	-89.938	38.688	-89.938	38.813	-89.938
38.313	-89.813	38.438	-89.813	38.563	-89.813	38.688	-89.813	38.813	-89.813

## APPENDIX B: GENERAL MFGEV MODEL

In what follows, we discuss how to fully exploit the information content of covariates sampled at a higher frequency than that of the block maxima.

Consider  $k$  covariates where  $\mathbf{x}_{j,t}^{(q_j)} = (x_{j,t,1}^{(q_j)}, \dots, x_{j,t,q}^{(q_j)})'$  is a vector of observations sampled  $q_j$  times within block  $t$  for the  $j$ th covariate, with  $j = \{1, \dots, k\}$ . We let the block maxima  $Y_t \sim H(y; \mathbf{x}_{1,t}^{(q_1)}, \dots, \mathbf{x}_{k,t}^{(q_k)} | \boldsymbol{\theta})$  with

$$(7) \quad \begin{aligned} \mu_t &= g_\mu \left( \kappa_0 + \sum_{j=1}^k \kappa_j \mathbf{w}(\phi_j) \cdot \mathbf{x}_{j,t}^{(q_j)} \right) \\ \sigma_t &= g_\sigma \left( \gamma_0 + \sum_{j=1}^k \gamma_j \mathbf{w}(\phi_j) \cdot \mathbf{x}_{j,t}^{(q_j)} \right) \\ \xi_t &= g_\xi \left( \zeta_0 + \sum_{j=1}^k \zeta_j \mathbf{w}(\phi_j) \cdot \mathbf{x}_{j,t}^{(q_j)} \right) \end{aligned}$$

where  $g_\mu(\cdot)$ ,  $g_\sigma(\cdot)$ ,  $g_\xi(\cdot)$  are functions that can be used to constrain the parameter space,  $\mathbf{w}(\phi_j) = (w(1|\phi_j), \dots, w(q|\phi_j))' \in \mathbb{R}^q$  is a vector of weights obtained from a parametric

weighting function  $\mathbf{w}(\cdot|\phi) \in (0, 1)$  such that  $\|\mathbf{w}(\phi_j)\|_1 = 1$ ,  $\cdot$  denotes the dot product, and  $\theta = (\kappa, \gamma, \zeta, \phi) \in \mathbb{R}^p$  is a vector of parameters. We call our model the Mixed-Frequency GEV (MFGEV) model. Of course, including same-frequency terms, i.e. with  $q = 1$ , is possible.

Let  $Y_{i,t}$  and  $(\mathbf{x}_{1,i,t}^{(q_1)}, \dots, \mathbf{x}_{k,i,t}^{(q_k)})$  be the maxima and the  $k$  covariates from the  $t$ th block at the  $i$ th location, respectively, with  $t \in \{1, \dots, m\}$  and  $i \in \{1, \dots, l\}$ . At each location in the homogeneous area, we can define general pooled MFGEV model as  $Y_{i,t} \sim H(y; \mathbf{x}_{1,i,t}^{(q_1)}, \dots, \mathbf{x}_{k,i,t}^{(q_k)} | \theta)$  with

$$(8) \quad \begin{aligned} \mu_{i,t} &= \kappa_0 + \sum_{j=1}^k \kappa_j \mathbf{w}(\phi_j) \cdot \mathbf{x}_{j,i,t}^{(q_j)} \\ \sigma_{i,t} &= \exp\left(\gamma_0 + \sum_{j=1}^k \gamma_j \mathbf{w}(\phi_j) \cdot \mathbf{x}_{j,i,t}^{(q_j)}\right) \\ \xi_{i,t} &= \zeta_0 + \sum_{j=1}^k \zeta_j \mathbf{w}(\phi_j) \cdot \mathbf{x}_{j,i,t}^{(q_j)} \end{aligned}$$

where  $\theta = (\kappa, \gamma, \zeta, \phi)$  gathers the common slope and weighting parameters and  $h(y; x|\theta)$  the density of the GEV distribution,

$$h(y; x|\theta) = \frac{1}{\sigma(x;\theta)} \left(1 + \xi(x;\theta) \frac{y - \mu(x;\theta)}{\sigma(x;\theta)}\right)^{-1 - \frac{1}{\xi(x;\theta)}} \exp\left(1 + \xi(x;\theta) \frac{y - \mu(x;\theta)}{\sigma(x;\theta)}\right)^{-\frac{1}{\xi(x;\theta)}}.$$

Linear forms are used for  $g_\mu$  and  $g_\xi$ , while  $g_\sigma$  is chosen to guarantee a positive scale.

### APPENDIX C: SIMULATIONS

We conduct a simulation study in order to assess: (i) the finite sample properties of the QML estimator of our pooled MFGEV model; (ii) the validity of the bootstrap confidence interval obtained with the procedure described in Section 3.3. We generate sample maxima  $\mathbf{Y}_t = (Y_{1,t}, \dots, Y_{l,t})$  at  $l$  spatial locations for  $t = \{1, \dots, m\}$  according to the following model

$$\mathbf{Y}_t \sim \mathbf{C}_\alpha \left( H(y_1; \mathbf{x}_{1,t}^{(q)} | \theta), \dots, H(y_l; \mathbf{x}_{l,t}^{(q)} | \theta) \right)$$

where  $\mathbf{C}_\alpha$  is a copula characterizing the spatial dependence structure with dependence parameter  $\alpha$ , and  $H(y; \mathbf{x}_{i,t}^{(q)} | \theta)$  is the marginal GEV distribution with  $i \in \{1, \dots, l\}$ . We assume constant scale and tail parameters through time and space, i.e.  $\sigma_{i,t} = \exp(\gamma)$  and  $\xi_{i,t} = \xi$ , and time varying location parameters

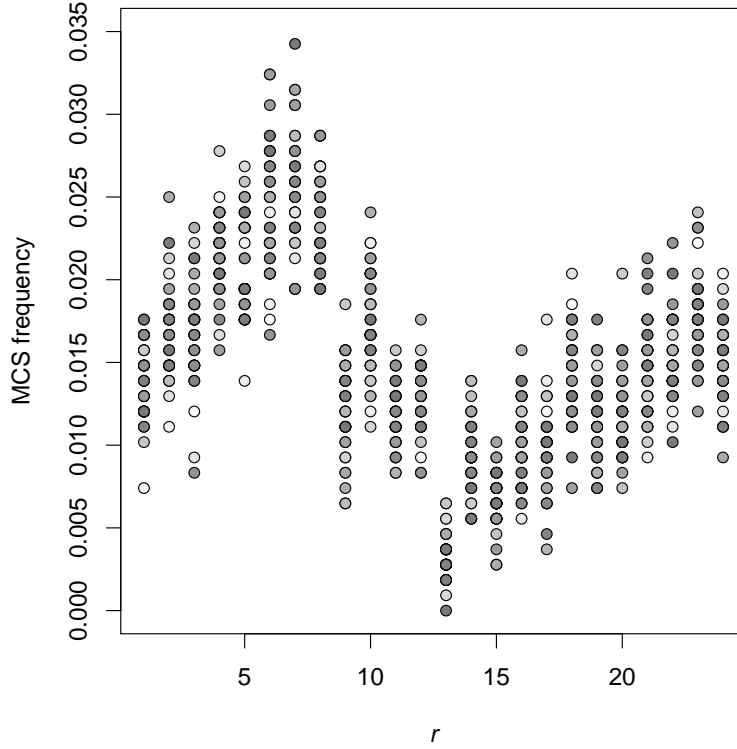
$$\mu_{i,t} = \kappa_0 + \kappa_1 \mathbf{w}(\phi) \cdot \mathbf{x}_{i,t}^{(q)} + \kappa_2 t$$

where  $\mathbf{w}(\phi) = (w(1|\phi), \dots, w(q|\phi))$  is a  $q$ -vector of weights and  $\mathbf{x}_{i,t}^{(q)} = (x_{i,t,1}^{(q)}, \dots, x_{i,t,q}^{(q)})$  is a covariate sampled  $q$  times within the  $t$ th block at the  $i$ th location. We let each component of  $\mathbf{x}_{i,t}^{(q)}$  to evolve according to the following model

$$(9) \quad \begin{aligned} x_{i,t,r}^{(q)} &= c z_{i,t,r}^{(q)}, \\ (z_{1,t,r}^{(q)}, \dots, z_{l,t,r}^{(q)}) &\sim \mathbf{C}_\rho^{\text{Gauss}}(\text{Po}(z_1|\lambda_r), \dots, \text{Po}(z_l|\lambda_r)) \end{aligned}$$

where  $r \in \{1, \dots, q\}$ ,  $c$  is a scaling constant,  $\text{Po}(z|\lambda)$  denotes the Poisson distribution with rate parameter  $\lambda$ , and  $\mathbf{C}_\rho^{\text{Gauss}}$  is a Gaussian copula with equi-correlation  $\rho$ . These dynamics are designed to match the empirical regularities observed in Section 4. Figure 9 depicts the average value of the covariate,  $\frac{1}{m} \sum_{t=1}^m x_{i,t,r}^{(q)}$ , at each  $i$ th location for each  $r \in \{1, \dots, q\}$  obtained from a random draw of the model setting  $m = 36$ ,  $l = 35$  and  $q = 24$ . The diurnal cycle in the covariate clearly emerges and resembles that empirically observed in Figure 4.

Fig 9: **Simulated MCS frequency.** Average value of the covariate at each  $i$ th location for hour  $r \in \{1, \dots, q\}$  obtained from a single draw of the model in (9), setting  $m = 36$ ,  $l = 35$ ,  $q = 24$ . A different shade of bullet is used for each location.



We generate  $R$  samples  $\left\{Y_{i,t}, \mathbf{x}_{i,t}^{(q)}\right\}_{i=1,t=1}^{l,m}$  of size  $m = 36$ ,  $l = 35$  and  $q = 24$ . We consider three copula functions to assess how the QML estimator and the bootstrap confidence interval behave under different assumptions on the spatial dependence of the maxima: an Independence copula ( $\mathbf{C}^{\text{Ind}}$ ) implying zero spatial dependence; a Gaussian copula ( $\mathbf{C}_{0.5}^{\text{Gauss}}$ ) with constant correlation coefficient equal to 0.5 across locations, implying a moderate spatial dependence but zero asymptotic dependence; a Gumbel copula ( $\mathbf{C}_2^{\text{Gumbel}}$ ) with dependence parameter  $\alpha = 2$  implying positive tail dependence  $\approx 0.6$ . We consider also two scenarios on the weighting parameter, i.e.  $\phi = \{0, 1\}$ , in order to assess the ability of our inference procedure to identify the situations requiring a mixed-frequency approach. The remaining model parameters are kept constant.

Tables 3 and 4 report the median estimates of the model parameters and the rejection probabilities for the 90%-, 95%- and 99%-confidence intervals over  $R = 100$  replications, with slightly heavy ( $\xi = 0.05$ ) and heavier ( $\xi = 0.2$ ) tails, respectively. Confidence intervals are built using  $B = 500$  bootstrap samples. In both tables, the results suggest that the QML estimator is centered on the true model parameters. Rejection probabilities are close to the correct size in general, and we only note a slight tendency of over-rejections on the scale ( $\gamma$ ) and tail ( $\xi$ ) parameters as spatial dependence increases, probably due to the model mis-specification. Finally, when  $\phi = 1$  we compute the rejection probabilities for the null assumption  $\phi_{\mathcal{H}_0} = 0$ . The test is very powerful when there is no spatial dependence, but decreases in power with increased dependence.

TABLE 3

**Performance of QML estimator with  $\xi = 0.05$ .** True parameter values, median estimates and rejection probabilities at the 10% ( $CI_{0.90}$ ), 5% ( $CI_{0.95}$ ), 1% ( $CI_{0.99}$ ) levels over  $B = 100$  replications for different three dependence structures, i.e.  $\mathbf{C}^{\text{Ind}}$ ,  $\mathbf{C}_{0.5}^{\text{Gauss}}$  and  $\mathbf{C}_2^{\text{Gumbel}}$ , and two assumptions on the weighting parameter, i.e.  $\phi = \{0, 1\}$ . When  $\phi = 1$  we also count the rejection rates for the null hypothesis  $\phi_{\mathcal{H}_0} = 0$ .

Independence ( $\mathbf{C}_\alpha = \mathbf{C}^{\text{Ind}}$ )													
	$\phi = 0$						$\phi = 1$						
	$\kappa_0$	$\kappa_1$	$\kappa_2$	$\gamma$	$\xi$	$\phi$	$\kappa_0$	$\kappa_1$	$\kappa_2$	$\gamma$	$\xi$	$\phi$	$\phi_{\mathcal{H}_0}$
True	5	1.65	0.015	1.2	0.05	0	5	1.65	0.015	1.2	0.05	1	0
Median	4.98	1.63	0.015	1.19	0.044	-0.02	4.99	1.64	0.016	1.2	0.04	1.01	
$CI_{0.9}$	0.12	0.14	0.10	0.11	0.11	0.15	0.16	0.14	0.09	0.11	0.10	0.13	0.97
$CI_{0.95}$	0.09	0.10	0.04	0.04	0.05	0.07	0.07	0.09	0.03	0.05	0.05	0.07	0.94
$CI_{0.99}$	0.01	0.03	0.01	0.01	0.02	0.04	0.00	0.03	0.01	0.01	0.02	0.01	0.84
Asymptotic independence ( $\mathbf{C}_\alpha = \mathbf{C}_{0.5}^{\text{Gauss}}$ )													
	$\kappa_0$	$\kappa_1$	$\kappa_2$	$\gamma$	$\xi$	$\phi$	$\kappa_0$	$\kappa_1$	$\kappa_2$	$\gamma$	$\xi$	$\phi$	$\phi_{\mathcal{H}_0}$
	$\kappa_0$	$\kappa_1$	$\kappa_2$	$\gamma$	$\xi$	$\phi$	$\kappa_0$	$\kappa_1$	$\kappa_2$	$\gamma$	$\xi$	$\phi$	$\phi_{\mathcal{H}_0}$
True	5	1.65	0.015	1.2	0.05	0	5	1.65	0.015	1.2	0.05	1	0
Median	4.91	1.62	0.019	1.16	0.048	-0.04	4.82	1.64	0.019	1.16	0.04	0.98	
$CI_{0.9}$	0.09	0.13	0.10	0.23	0.20	0.12	0.08	0.15	0.10	0.23	0.20	0.08	0.49
$CI_{0.95}$	0.04	0.08	0.05	0.21	0.14	0.06	0.03	0.10	0.06	0.21	0.12	0.06	0.39
$CI_{0.99}$	0.00	0.01	0.01	0.11	0.07	0.02	0.00	0.04	0.01	0.11	0.06	0.01	0.23
Asymptotic dependence ( $\mathbf{C}_\alpha = \mathbf{C}_2^{\text{Gumbel}}$ )													
	$\kappa_0$	$\kappa_1$	$\kappa_2$	$\gamma$	$\xi$	$\phi$	$\kappa_0$	$\kappa_1$	$\kappa_2$	$\gamma$	$\xi$	$\phi$	$\phi_{\mathcal{H}_0}$
	$\kappa_0$	$\kappa_1$	$\kappa_2$	$\gamma$	$\xi$	$\phi$	$\kappa_0$	$\kappa_1$	$\kappa_2$	$\gamma$	$\xi$	$\phi$	$\phi_{\mathcal{H}_0}$
True	5	1.65	0.015	1.2	0.05	0	5	1.65	0.015	1.2	0.05	1	0
Median	5.18	1.66	0.021	1.17	0.04	-0.08	4.87	1.62	0.022	1.17	0.04	0.86	
$CI_{0.9}$	0.10	0.09	0.11	0.17	0.25	0.08	0.10	0.08	0.11	0.20	0.24	0.08	0.33
$CI_{0.95}$	0.04	0.06	0.07	0.15	0.15	0.05	0.06	0.06	0.06	0.14	0.16	0.04	0.21
$CI_{0.99}$	0.02	0.03	0.02	0.05	0.05	0.02	0.02	0.03	0.02	0.05	0.05	0.01	0.06

**Acknowledgments.** The authors wish to thank the Associate Editor and two anonymous referees for helpful comments that improved the paper. The authors also wish to thank Ruby Leung and Zhe Feng for providing the data and helpful discussion.

**Funding.** The first author was supported by the Natural Sciences and Engineering Research Council of Canada RGPIN-2016-04114 and the HEC Foundation.



TABLE 4

**Performance of QML estimator with  $\xi = 0.2$ .** True parameter values, median estimates and rejection probabilities at the 10% ( $CI_{0.90}$ ), 5% ( $CI_{0.95}$ ), 1% ( $CI_{0.99}$ ) levels over  $B = 100$  replications for different three dependence structures, i.e.  $\mathbf{C}^{\text{Ind}}$ ,  $\mathbf{C}_{0.5}^{\text{Gauss}}$  and  $\mathbf{C}_2^{\text{Gumbel}}$ , and two assumptions on the weighting parameter, i.e.  $\phi = \{0, 1\}$ . When  $\phi = 1$  we also count the rejection rates for the null hypothesis  $\phi_{\mathcal{H}_0} = 0$ .

	Independence ( $\mathbf{C}_\alpha = \mathbf{C}^{\text{Ind}}$ )													
	$\phi = 0$						$\phi = 1$							
	$\kappa_0$	$\kappa_1$	$\kappa_2$	$\gamma$	$\xi$	$\phi$	$\kappa_0$	$\kappa_1$	$\kappa_2$	$\gamma$	$\xi$	$\phi$	$\phi_{\mathcal{H}_0}$	
True	5	1.65	0.015	1.2	0.2	0	5	1.65	0.015	1.2	0.2	1	0	
Median	4.96	1.64	0.015	1.20	0.19	-0.01	4.97	1.66	0.016	1.2	0.19	1.01		
$\text{CI}_{0.9}$	0.12	0.14	0.10	0.08	0.10	0.15	0.12	0.14	0.09	0.09	0.10	0.12	0.99	
$\text{CI}_{0.95}$	0.07	0.08	0.04	0.03	0.05	0.06	0.08	0.08	0.04	0.02	0.05	0.06	0.98	
$\text{CI}_{0.99}$	0.01	0.03	0.03	0.00	0.01	0.04	0.00	0.02	0.01	0.00	0.01	0.01	0.92	
Asymptotic independence ( $\mathbf{C}_\alpha = \mathbf{C}_{0.5}^{\text{Gauss}}$ )														
	$\kappa_0$	$\kappa_1$	$\kappa_2$	$\gamma$	$\xi$	$\phi$	$\kappa_0$	$\kappa_1$	$\kappa_2$	$\gamma$	$\xi$	$\phi$	$\phi_{\mathcal{H}_0}$	
True	5	1.65	0.015	1.2	0.2	0	5	1.65	0.015	1.2	0.2	1	0	
Median	4.95	1.58	0.02	1.16	0.19	-0.04	4.82	1.67	0.02	1.16	0.19	1.01		
$\text{CI}_{0.9}$	0.08	0.14	0.11	0.25	0.22	0.11	0.08	0.12	0.11	0.24	0.22	0.10	0.56	
$\text{CI}_{0.95}$	0.03	0.08	0.06	0.19	0.17	0.08	0.03	0.10	0.06	0.20	0.17	0.06	0.46	
$\text{CI}_{0.99}$	0.00	0.03	0.01	0.10	0.08	0.01	0.00	0.04	0.01	0.07	0.08	0.02	0.27	
Asymptotic dependence ( $\mathbf{C}_\alpha = \mathbf{C}_2^{\text{Gumbel}}$ )														
	$\kappa_0$	$\kappa_1$	$\kappa_2$	$\gamma$	$\xi$	$\phi$	$\kappa_0$	$\kappa_1$	$\kappa_2$	$\gamma$	$\xi$	$\phi$	$\phi_{\mathcal{H}_0}$	
True	5	1.65	0.015	1.2	0.2	0	5	1.65	0.015	1.2	0.2	1	0	
Median	5.08	1.64	0.02	1.18	0.2	-0.07	4.88	1.67	0.019	1.18	0.2	0.93		
$\text{CI}_{0.9}$	0.09	0.11	0.10	0.18	0.22	0.10	0.14	0.08	0.12	0.18	0.23	0.11	0.45	
$\text{CI}_{0.95}$	0.05	0.07	0.06	0.13	0.14	0.07	0.04	0.05	0.05	0.13	0.15	0.05	0.26	
$\text{CI}_{0.99}$	0.02	0.02	0.02	0.04	0.05	0.01	0.03	0.02	0.02	0.04	0.05	0.01	0.14	